Nature of magnetic phase transitions and spin-driven ferroelectricity in $BaHoFeO_4$

N. T. Dang [1,2,*] D. P. Kozlenko [3] T. P. Hoang [1,2,†] A. V. Rutkauskas,[3] T. N. Vershinina [3] S. E. Kichanov [3] D. T. Khan [4] L. T. P. Thao [4] T. L. Phan [5] N. Tran [1,2] E. V. Dyuzheva-Maltseva,[6] C. Kadlec [7] F. Kadlec [7] T. Kmječ [8] J. Kohout [8] V. Chlan [8,‡] and M. H. Phan [9,§]

[1]*Institute of Research and Development, Duy Tan University, 550000 Danang, Vietnam*
[2]*Faculty of Natural Sciences, Duy Tan University, 550000 Danang, Vietnam*
[3]*Frank Laboratory of Neutron Physics, Joint Institute for Nuclear Research, 141980 Dubna, Russia*
[4]*The University of Danang–University of Science and Education, 550000 Danang, Vietnam*
[5]*Faculty of Engineering Physics and Nanotechnology, VNU-University of Engineering and Technology, 144 Xuan Thuy, Cau Giay, 100000 Hanoi, Vietnam*
[6]*Baikov Institute of Metallurgy and Materials Science, Russian Academy of Sciences, 119991 Moscow, Russia*
[7]*Institute of Physics of the Czech Academy of Sciences, Na Slovance 2, 182 00 Prague, Czech Republic*
[8]*Faculty of Mathematics and Physics, Charles University, V Holešovičkách 2, Prague 18000, Czech Republic*
[9]*Department of Physics, University of South Florida, Tampa, Florida 33620, USA*

(Received 9 May 2025; revised 28 July 2025; accepted 1 August 2025; published 15 August 2025)

$BaHoFeO_4$ is an emergent multiferroic material that exhibits unique magnetic-field (H)-induced ferroelectric behavior. However, the origin of this effect has remained elusive, due to the role of complex magnetic interactions in driving the system's behavior. To shed light on this, we investigated the magnetic structures of the material using neutron powder diffraction, as well as their magnetic-field-induced evolutions through a combination of complementary techniques, including magnetic measurements, Mössbauer spectroscopy, and terahertz time-domain spectroscopy. The orthorhombic crystal structure of the compound, characterized by the structural interconnection between two-dimensional Fe chains and Ho chains, remains stable upon cooling to 3 K. Below $T_{N1} \approx 50$ K, Fe^{3+} spins form a collinear incommensurate spin-density-wave antiferromagnetic order with a magnetic propagation vector $k_1 = (0, 0, 0.329)$, and the magnetic moments align along the b axis. Upon further cooling, the enhancement of the $3d$-$4f$ exchange coupling induces long-range order in the Ho sublattice below 25 K, transforming the magnetic structure into a noncollinear commensurate antiferromagnetic order with $k_2 = (0.5, 0, 0.5)$, with all Fe and Ho moments lying in the ac plane. As the temperature decreases further, strengthening of the $4f$-$4f$ interactions leads to the emergence of a new commensurate antiferromagnetic order with a magnetic propagation vector $k_3 = (0, 0, 0.5)$ at 3 K, coexisting with the antiferromagnetic structure associated with k_2. Similar to the incommensurate spin-density-wave structure, the Ho and Fe spins in the k_3 phase are oriented along the b axis, with their magnetic moments modulated along the c axis. The spin configuration of the Ho rings is highly sensitive to temperature and magnetic field, in contrast to the more robust spin configuration of the Fe rings. We attribute the H-induced magnetic and ferroelectric transitions in $BaHoFeO_4$ to the H-induced modifications in the Ho sublattice. Two metamagnetic phase transitions occur at $H_1 \approx 1$ T and $H_2 \approx 2$ T, associated with a spin-flop transition of the Ho magnetic sublattice. The H-induced canted magnetic configuration in the Ho rings above H_1 drives the H-induced ferroelectricity in $BaHoFeO_4$. This is subsequently suppressed by the growth of a higher-field paraelectric antiferromagnetic phase, characterized by a fully ferromagnetic arrangement of the Ho chains above H_2. Our study provides important insights into the origins of the metamagnetic phase transitions and the associated magnetoelectric effects.

DOI: 10.1103/xz8c-3fp3

I. INTRODUCTION

The discovery of spin-driven ferroelectricity and unique magnetic phase transitions in $BaRFeO_4$ (where R represents rare-earth elements) has garnered significant scientific attention due to the fascinating interplay between structural, magnetic, and electronic properties in these materials, making them ideal platforms for exploring novel multiferroic behaviors [1–6]. A key feature of $BaRFeO_4$ is the geometric frustration intrinsic to its crystal structure, which arises from the arrangement of $Fe^{3+}O_6$ octahedra and $Fe^{3+}O_5$ pyramids, forming Fe_4O_{18} rings (Fig. 1). These rings stack along the b axis, forming two-dimensional magnetic chains. In parallel, the RO_7 polyhedra form two-dimensional chains along the same axis through edge sharing, linking the Fe chains. This structural interconnection between Fe chains and R

*Contact author: dangngoctoan1@duytan.edu.vn
†Contact author: hoangtrongphuc@duytan.edu.vn
‡Contact author: chlan@mbox.troja.mff.cuni.cz
§Contact author: phanm@usf.edu

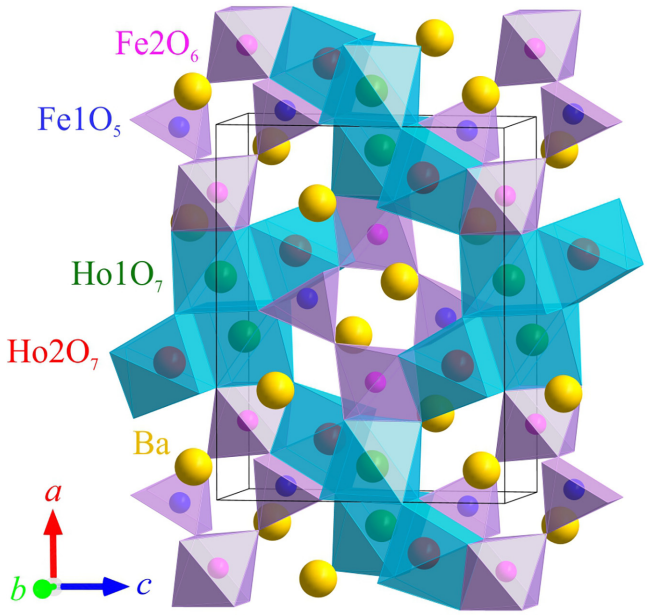

FIG. 1. Scheme of the orthorhombic *Pnma* crystal structure of $BaHoFeO_4$.

chains gives rise to intricate magnetic interactions and exotic behaviors.

For $BaYFeO_4$ with pure $3d$ electron magnetism, the Fe sublattice exhibits a long-range collinear spin-density-wave (SDW) antiferromagnetic (AFM) order with orientation of the Fe^{3+} magnetic moments along the chain direction (b axis) and modulation along the c axis below $T_{N1} \approx 48$ K [7–10]. Below $T_{N2} \approx 33$ K, this magnetic order transforms into a noncollinear cycloidal AFM order, with Fe spins rotating within the bc plane and accompanied by the appearance of residual electric polarization [8]. All magnetic structures are incommensurate with propagation vectors $k = (0, 0, k_z \sim 1/3)$ [7,11]. It is worth noting that the $3d$-$4f$ magnetic exchange interaction plays a critical role in shaping the magnetic and ferroelectric properties of the systems, resulting in their rich diversity. Replacing Y by magnetic rare-earth elements, such as Tm, Yb, and Er, does not modify the SDW structure formed below T_{N1}, but it alters the AFM structure appearing below T_{N2} [4,5]. For R = Yb, Tm, a cycloidal spiral magnetic structure, comprising both SDW and cycloidal components, was observed [4]. Additionally, the cycloidal magnetic structure for R = Yb has a different irreducible representation than that of R = Y and R = Tm compounds [4]. In contrast, $BaErFeO_4$ exhibits a commensurate (CM) AFM phase with a propagation vector $k = (0.5, 0, 0.5)$ with the Fe and Er magnetic moments ordered in the ac plane below T_{N2}, likely formed due to $3d$-$4f$ exchange interactions [5]. The competition between $3d$-$4f$ and $4f$-$4f$ interactions results in the complex magnetic structures within the R magnetic sublattice [4,5].

Moreover, $BaRFeO_4$ compounds with magnetic R ions exhibit a complex magnetic response to external magnetic fields, characterized by multiple metamagnetic phase transitions that are notably absent in $BaYFeO_4$ [2,3,6]. Interestingly, in $BaHoFeO_4$, an H-induced ferroelectric polarization appears above the metamagnetic transition field ($\mu_0 \geqslant 1.5$ T) [3]. As μ_0 increases to 2 T, the ferroelectric polarization grows, then weakens sharply beyond this field, disappearing entirely above 5 T [3]. Such an unusual ferroelectric behavior is likely related to the metastable phase transitions under magnetic fields. Despite these compelling observations, the detailed spin structures of both the magnetic ground state and the field-induced phases remain unclear. This knowledge gap is critical to unraveling the mechanisms behind the observed magnetoelectric coupling and related phenomena in $BaHoFeO_4$.

In this study, we have systematically investigated the magnetic structure and field-induced behavior of $BaHoFeO_4$ using a suite of complementary techniques, including neutron diffraction, magnetic measurements, Mössbauer spectroscopy, and terahertz time-domain spectroscopy. Our findings provide deeper insights into the interplay of spin, lattice arrangements, and ferroelectric polarization in this fascinating multiferroic material.

II. EXPERIMENTAL DETAILS

A polycrystalline $BaHoFeO_4$ sample was prepared from stoichiometric mixtures of $BaCO_3$, Ho_2O_3, and Fe_2O_3 (purchased from Sigma Aldrich, purities $\geqslant$99.9%) by the solid-state reaction method as described in Ref. [7].

The crystal structure and phase composition of the synthesized compound were determined using a D8 Advance Eco (Bruker) X-ray diffractometer (equipped with a Cu $K\alpha$ radiation source: $\lambda_1 = 1.5406$ Å, $\lambda_2 = 1.5444$ Å, and their intensity ratio $I_2/I_1 = 0.48$). The neutron powder diffraction (NPD) experiments were conducted on the DISK diffractometer (IR-8 stationary reactor, National Research Center Kurchatov Institute, Russia) using a constant wavelength of $\lambda = 2.41$ Å. The NPD patterns were collected over the temperature range 3–290 K for a 2θ range 3.0°–157.5° with a step width 0.088°, and analyzed using the Rietveld method with the fullprof suite [12].

Magnetic measurements were performed in a field range 0–9 T and at temperatures from 2 to 300 K using a Quantum Design Physical Property Measurement System with the Vibrating Sample Magnetometer. The powdered sample of $BaHoFeO_4$ was tightly packed into a gelcap to suppress grain rotation during these magnetic measurements. For Mössbauer measurements, the powdered sample of $BaHoFeO_4$ was mixed with wax and pressed into a 12-mm-diameter tablet. The ^{57}Fe Mössbauer spectra were collected in transmission geometry with a conventional spectrometer (WissEl GmbH, Germany) working in the constant-acceleration mode, equipped with a ^{57}Co(Rh) source. Calibration of the velocity scale was carried out using an α-Fe foil at room temperature, with isomer shift values given relative to the center of its Mössbauer spectrum. The spectra were acquired from 4.2 to 300 K and under external magnetic fields up to 6 T, oriented perpendicular to the γ-beam direction. Data analysis was performed using the confit [13] and mosswinn [14] fitting software.

Terahertz time-domain spectroscopy was based on measuring complex transmittance using two custom-made time-domain spectrometers. In the first setup, an electrically biased interdigitated large-area photoconductive emitter was used for

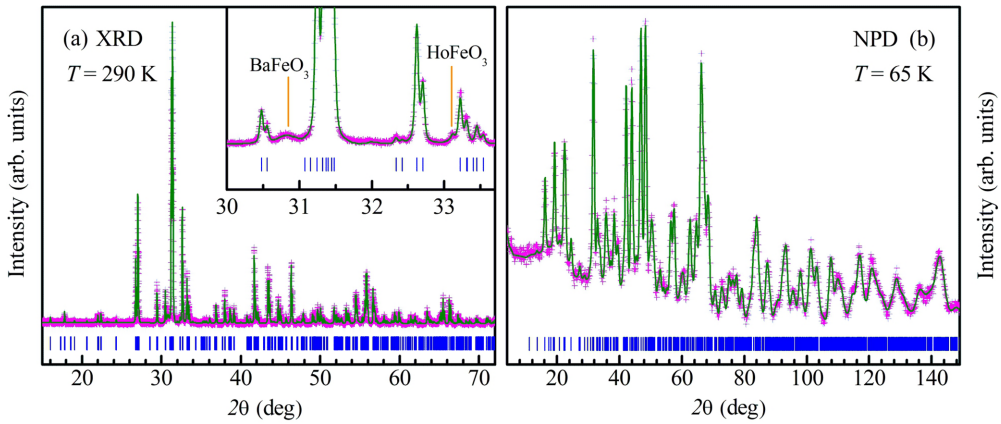

FIG. 2. (a) Room-temperature XRD and (b) 65-K NPD patterns of $BaHoFeO_4$, refined using the Rietveld method. Experimental data points and calculated profiles are displayed, with tick marks below indicating the nuclear peak positions for the *Pnma* orthorhombic phase. Inset of (a): enlarged view of the XRD pattern region showing reflections from cubic $BaFeO_3$ and orthorhombic $HoFeO_3$.

generating the broadband terahertz pulses and a [011] ZnTe crystal for their phase-sensitive detection. The sample was cooled in a He-flow optical cryostat (Optistat, Oxford instruments) down to $T = 10$ K. In the second setup, terahertz pulses were generated and detected using commercial fiber-coupled photoconductive switches operating with a femtosecond optical fiber laser system (TeraSmart, Menlo Systems GmbH). The sample was placed in an Oxford Instruments Spectromag He-bath cryostat fitted with mylar windows and a superconducting coil, able to provide a magnetic field of up to $\mu_0 H = 7$ T, and to cool the sample down to $T = 2$ K. For terahertz measurements, the $BaHoFeO_4$ powder was pressed to a pellet about 6 mm in diameter with a 1 mm thickness.

III. RESULTS AND DISCUSSION

A. Crystal structure and magnetic phase transitions

The Rietveld refinements of X-ray diffraction (XRD) and NPD data have revealed that $BaHoFeO_4$ adopts the orthorhombic *Pnma* crystal structure, which remains unchanged upon cooling to 3 K (see Fig. 2). Additionally, small amounts of impurities, $BaFeO_3$ at 2.1(3) wt % and $HoFeO_3$ at 1.6(3) wt %, have been detected [Fig. 2(a)]. The structural details of the paramagnetic phase of $BaHoFeO_4$ at $T = 65$ K, obtained from NPD data, are listed in Table I.

Furthermore, the macroscopic magnetic characteristics of $BaHoFeO_4$ have been investigated using temperature-dependent zero-field-cooling (ZFC) and field-cooling (FC) magnetization curves measured at 100 Oe [Fig. 3(a)]. Previous studies have shown that $BaHoFeO_4$ undergoes three magnetic phase transitions at $T_{N1} \sim 52.8$ K, $T_{N2} \sim 36.4$ K, and $T_{N3} \sim 6.8$ K [2,3,6]. The first two were attributed to changes in the spin structure of Fe^{3+} spins, while the third was linked to the AFM ordering of the Ho^{3+} sublattice [2,3,6]. However, our magnetic data reveal only a small cusp at $T_{N1} \sim 50$ K, in contrast to the sharp peaks observed at the corresponding transition points in the isostructural $BaYFeO_4$ [1,7,8,10,11,15]. This difference can be attributed to the strong paramagnetic contribution from Ho^{3+} ions, masking the magnetic signals from the Fe sublattice. Interestingly, the FC and ZFC magnetization versus temperature $M(T)$ curves [Fig. 3(a)] start to bifurcate at 220 K, coinciding with the deviation point between the inverse susceptibility versus temperature curve, $\chi^{-1}(T)$, and its Curie-Weiss fitting curves. This behavior can be attributed to the onset of short-range AFM correlations inside the $[Fe_4O_{18}]_n$ columns, mirroring observations in

TABLE I. Refined structural parameters and relevant interatomic distances of $BaHoFeO_4$ at 65 K. Space group *Pnma*, $a = 13.1239(16)$ Å, $b = 5.6900(6)$ Å, and $c = 10.2346(14)$ Å. $\chi^2 = 2.12$, $R_p = 3.08\%$, $R_{wp} = 3.88\%$; $R_{expt} = 2.67\%$, $R_B = 3.21\%$.

Atom	Site	x	y	z	B (Å^2)
Ba1	4*c*	0.2135(9)	0.25	0.6767(11)	0.034(79)
Ba2	4*c*	0.4205(11)	0.25	0.3923(13)	= *B*(Ba1)
Ho1	4*c*	0.5869(6)	0.75	0.9872(8)	0.030(69)
Ho2	4*c*	0.3571(5)	0.75	0.8091(7)	= *B*(Ho1)
Fe1	4*c*	0.0317(5)	0.75	0.2123(6)	0.075(54)
Fe2	4*c*	0.1889(5)	0.25	0.0242(6)	= *B*(Fe1)
O1	4*c*	0.5873(9)	0.25	0.6175(10)	0.441(43)
O2	4*c*	0.2929(9)	0.25	0.1835(10)	= *B*(O1)
O3	8*d*	0.0052(6)	0.5095(15)	0.3557(6)	= *B*(O1)
O4	8*d*	0.2164(5)	0.5080(13)	0.4411(7)	= *B*(O1)
O5	8*d*	0.1104(5)	0.0016(17)	0.1290(7)	= *B*(O1)

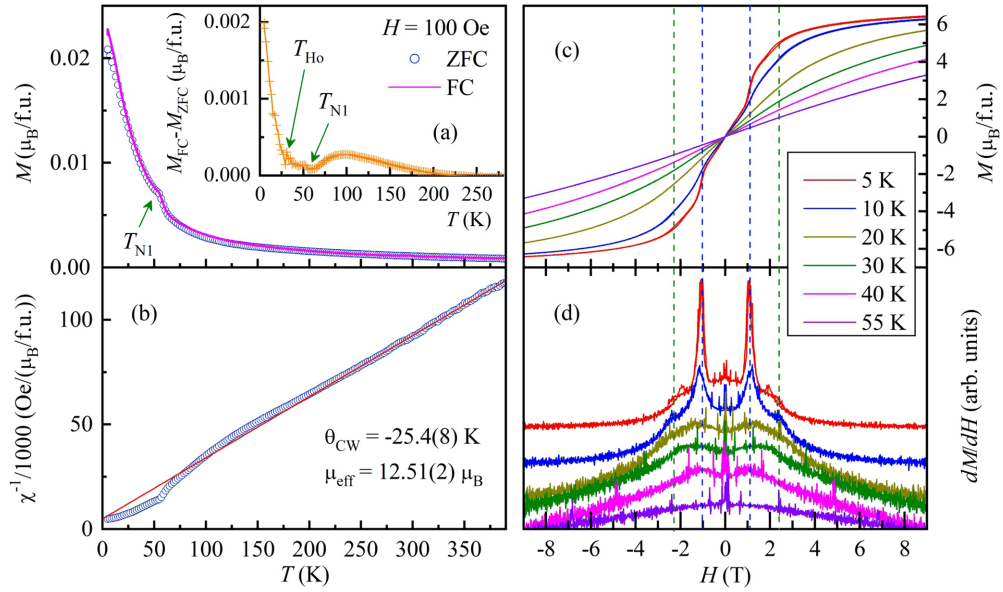

FIG. 3. (a) ZFC and FC magnetic susceptibility $\chi(T)$ of $BaHoFeO_4$, collected under $H = 100$ Oe. Inset: Curie-Weiss fitting of the experimental data χ^{-1} vs T. (b) $M(H)$ loops at selected temperatures. (c) Corresponding dM/dH curves, enlarged and shifted vertically for clarity.

$BaYFeO_4$ [7,11,15]. As the temperature decreases further, the bifurcation becomes more pronounced, reaching a maximum near 100 K, which likely corresponds to enhanced interactions between the magnetic columns. At T_{N1}, this bifurcation diminishes, followed by a slight increase upon further cooling to 25 K, labeled as T_{Ho}. Below T_{Ho}, a sharp upturn in the bifurcation curve is observed, which can be attributed to the emergence of long-range magnetic ordering involving Ho^{3+} ions, as confirmed by the NPD and Mössbauer results, which are presented and discussed below.

Moreover, fitting the $\chi^{-1}(T)$ data to the Curie-Weiss law in the paramagnetic range 220–390 K yields an effective magnetic moment of $12.51(2)\mu_B$, which agrees well with the theoretical value of $12.16\mu_B$ [Fig. 3(b)]. The negative Curie-Weiss temperature $\theta_{CW} = -25.4(8)$ K indicates the dominance of AFM interactions in the material. Additionally, the $M(H)$ isothermal magnetization curves [Fig. 3(c)] and their first derivatives [Fig. 3(d)] reveal two field-induced metamagnetic transitions around $\mu_0 H_1 \approx 1$ T and $\mu_0 H_2 \approx 2$ T [Figs. 3(c) and 3(d)]. This behavior contrasts with the linear $M(H)$ curves observed in $BaYFeO_4$ at low temperatures, which lack any metamagnetic transitions [7], implying that the H-induced transitions in $BaHoFeO_4$ are most likely associated with the Ho sublattice. As shown in Figs. 3(c) and 3(d), the magnetization at 5 K increases almost linearly with increasing magnetic field below H_1 and exhibits a sharp jump at H_1, followed by a gradual rise with further increasing H up to H_2, after which it tends to saturate. The saturated magnetization of $\sim 6.5\mu_B$ at 5 K is significantly smaller than the free-ion value of $10.6\mu_B$ for Ho^{3+}, suggesting a substantial fraction of Ho^{3+} disordered spins.

These observations also suggest a spin-flop transition in the Ho sublattice, which is expected for the AFM spin configuration of Ho spins as determined by NPD measurements (Fig. 6) [16,17]. Here, H_1 and H_2 can be considered as the spin-flop starting and ending critical fields, respectively [16,17]. Notably, the $M(H)$ curves for the decreasing and increasing field regimes at 5 K do not coincide during the spin-flop process, indicating a first-order transition. Both the metamagnetic transitions are broad above 10 K, which is typical for polycrystalline samples. Upon further cooling, the lower-field transition becomes sharp, which can be attributed to enhanced $4f$-$4f$ interactions, consistent with the NPD results. Moreover, the higher-field transition is visible at 30 K but not at 40 K, while the lower-H transition still persists at 40 K, above T_{N2}, suggesting a presence of short-range correlations between Ho^{3+} ions.

B. Zero-field magnetic structures probed by neutron diffraction

In order to clarify the character of magnetically ordered states formed in $BaHoFeO_4$ in the absence of magnetic fields, the neutron powder diffraction experiments were performed at selected temperatures around the metamagnetic phase transition points detected above. As shown in the inset of Fig. 4(a), the NPD pattern at 42 K displays magnetic contributions at 2θ positions of 13.4°, 13.9°, and 20.7° compared to the paramagnetic pattern at 65 K, which can be indexed to an incommensurate magnetic propagation vector $k_1 = (0, 0, 0.329(7))$. For this k_1 value and the *Pnma* space group, representation analysis predicts four irreducible representations (irreps) for the $4c$ sites occupied by Fe or Ho ions: $\mathbf{\Gamma} = 1\mathbf{\Gamma_1} + 2\mathbf{\Gamma_2} + 1\mathbf{\Gamma_3} + 2\mathbf{\Gamma_4}$, as outlined in Table II. Each unique $4c$ site splits into two orbits, with magnetic symmetry coupling only between pairs separated by $\Delta z = 0.5$; for instance, Fe/Ho_1 $(\boldsymbol{x},\boldsymbol{y},\boldsymbol{z})$ pairs with Fe/Ho_2 $(-\boldsymbol{x}+\mathbf{0.5}, -\boldsymbol{y}, \boldsymbol{z}+\mathbf{0.5})$, and Fe/Ho_3 $(-\boldsymbol{x}, \boldsymbol{y}+\mathbf{0.5}, -\boldsymbol{z})$ with Fe/Ho_4 $(\boldsymbol{x}+\mathbf{0.5}, -\boldsymbol{y}+\mathbf{0.5}, -\boldsymbol{z}+\mathbf{0.5})$. It means that there is no symmetry coupling within individual Fe/Ho rings, but the interchain coupling is governed by magnetic symmetries within a given irrep. A trial-and-error fitting approach

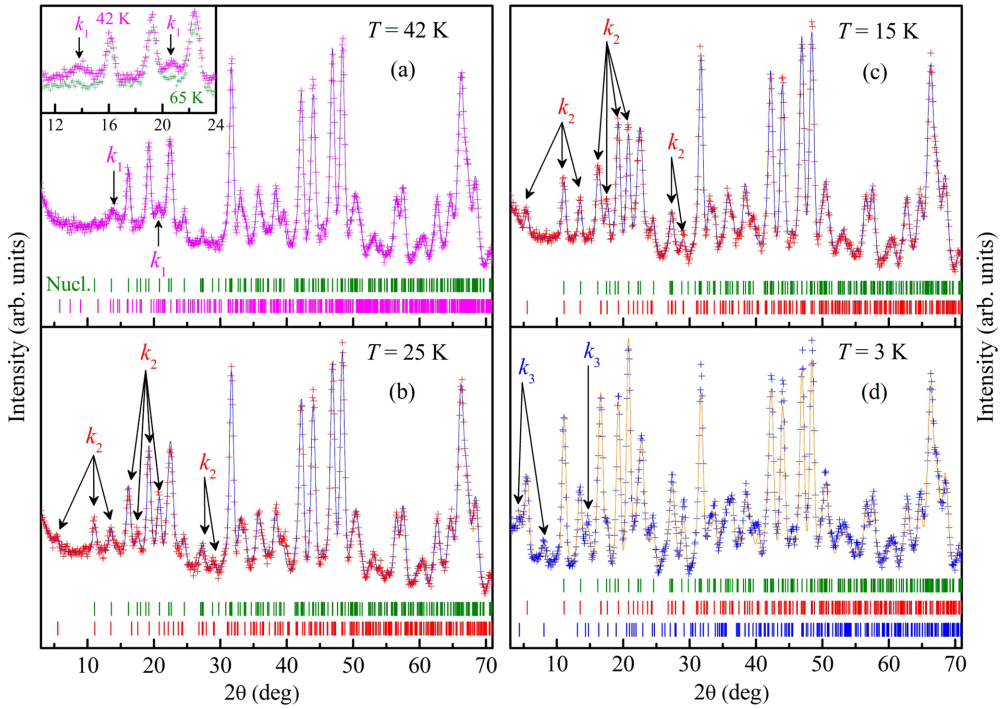

FIG. 4. NPD patterns of $BaHoFeO_4$ at 42 K (a), 25 K (b), 15 K (c), and 3 K (d). Experimental data points and calculated profiles are displayed. Vertical ticks at the bottom denote the positions of nuclear and magnetic reflections.

has revealed that the collinear SDW magnetic structure corresponding to $\mathbf{\Gamma_3}$ provides the best match with the experimental NPD data [Fig. 4(a)]. This magnetic phase is associated solely with Fe ions, and the details of its magnetic structure refinement are listed in Table III. Due to strong AFM intrachain interactions, the magnetic moments and the magnetic phase are constrained to be the same for Fe ions within the same Fe_4O_{18} ring. As depicted in Fig. 5, in the SDW structure at 42 K, the Fe^{3+} moments, with a value of $2.75(6)\mu_B$ at the $Fe1_1$ and $Fe2_1$ sites (Table III), are aligned along the b axis and modulated along the c axis, the direction of the propagation vector k_1.

Upon further cooling, the NPD pattern at 25 K, below T_{N2}, shows sharp changes [see Fig. 4(b)], including the appearance of new magnetic peaks at 5.51°, 11.08°, and 17.61° along with enhanced magnetic contributions to the intensity of the nuclear peaks at 13.52°, 20.79°, 27.26°, and 29.18°. These magnetic peaks can be fully indexed to a CM magnetic propagation vector $k_2 = (0.5, 0, 0.5)$, similar to that observed for $BaErFeO_4$ [5]. Using the representation analysis approach

TABLE II. Irreducible representations (IR) and Basis vectors (BsV) for the 4*c* sites of Fe atoms in the *Pnma* space group with the magnetic propagation $k = (0, 0, k_z \sim 0.33)$: $\mathbf{\Gamma} = 1\mathbf{\Gamma_1} + 2\mathbf{\Gamma_2} + 1\mathbf{\Gamma_3} + 2\mathbf{\Gamma_4}$. Each of the nonequivalent Fe and Ho ions were split into two orbits. Only the pairs separated by $\Delta z = 0.5$ are coupled by magnetic symmetry; for example, Fe/Ho_1 $(\boldsymbol{x}, \boldsymbol{y}, \boldsymbol{z})$ with Fe/Ho_2 $(-\boldsymbol{x} + \mathbf{0.5}, -\boldsymbol{y}, \boldsymbol{z} + \mathbf{0.5})$ and Fe/Ho_3 $(-\boldsymbol{x}, \boldsymbol{y} + \mathbf{0.5}, -\boldsymbol{z})$ with Fe/Ho_4 $(\boldsymbol{x} + \mathbf{0.5}, -\boldsymbol{y} + \mathbf{0.5}, -\boldsymbol{z} + \mathbf{0.5})$. In the table, $a = \mathrm{Re}(\varepsilon) = \cos(\pi k_z)$ and $b = \mathrm{Im}(\varepsilon) = \sin(\pi k_z)$, where $\varepsilon = \exp(i\pi k_z)$ is the phase factor.

IR	BsV	Orbit 1: *x*, *y*, *z* Orbit 2: $-\boldsymbol{x}, \boldsymbol{y} + \mathbf{0.5}, -\boldsymbol{z}$	$-\boldsymbol{x} + \mathbf{0.5}, -\boldsymbol{y}, \boldsymbol{z} + \mathbf{0.5}$ $\boldsymbol{x} + \mathbf{0.5}, -\boldsymbol{y} + \mathbf{0.5}, -\boldsymbol{z} + \mathbf{0.5}$
$\mathbf{\Gamma_1}$	Ψ_1	Re (0 1 0)	(0 $-a$ 0)
		Im (0 0 0)	(0 b 0)
$\mathbf{\Gamma_2}$	Ψ_{21}	Re (1 0 0)	($-a$ 0 0)
		Im (0 0 0)	(b 0 0)
	Ψ_{22}	Re (0 0 1)	(0 0 a)
		Im (0 0 0)	(0 0 $-b$)
$\mathbf{\Gamma_3}$	Ψ_3	Re (0 1 0)	(0 a 0)
		Im (0 0 0)	(0 $-b$ 0)
$\mathbf{\Gamma_4}$	Ψ_{41}	Re (1 0 0)	(a 0 0)
		Im (0 0 0)	($-b$ 0 0)
	Ψ_{42}	Re (0 0 1)	(0 0 $-a$)
		Im (0 0 0)	(0 0 b)

TABLE III. Details of magnetic structures of $BaHoFeO_4$ refined from NPD data at 42, 25, 15, and 3 K.

$T = 42$ K: $\chi^2 = 2.56$, $R_p = 8.34\%$, $R_{wp} = 9.30\%$, $R_{expt} = 5.82\%$, $R_B = 3.14\%$, $R_M = 18.97\%$
$k_1 = (0, 0, 0.329(7))$; irrep: $\mathbf{\Gamma_3}$
$Fe1_1$, $Fe1_3$: $M = (0, 2.75(6), 0)\mu_B$, $\delta = 0$
$Fe2_1$, $Fe2_3$: $M = (0,-2.75(6),0)\mu_B$, $\delta = 0$

$T = 25$ K: $\chi^2 = 2.46$, $R_p = 8.23\%$, $R_{wp} = 9.14\%$, $R_{expt} = 5.83\%$, $R_B = 3.09\%$, $R_M = 11.5\%$
$k_2 = (0.5, 0, 0.5)$; irrep: $\mathbf{\Gamma_7}$
$Fe1_1$: C1 = −1.57(23), C2 = 1.51(22), C3 = C4 = 0, $\delta = 0.125$, $M = (-1.11(16), 0, 1.07(16))\mu_B$
$Fe2_1$: C1 = 1.57(23), C2 = −1.51(22), C3 = C4 = 0, $\delta = 0.125$, $M = (1.11(16),0,-1.07(16))\mu_B$
$Ho1_1$: C1 = 1.96(33), C2 = 1.03(59), C3 = C4 = 0, $\delta = -0.06(3)$, $M = (1.84(31),0,0.97(54))\mu_B$
$Ho2_1$: C1 = 1.54(22), C2 = −0.52(24), C3 = C4 = 0, $\delta = 0.59(3)$, $M = (1.29(18),0,-0.43(20))\mu_B$

$T = 15$ K: $\chi^2 = 2.84$, $R_p = 8.74\%$, $R_{wp} = 9.98\%$; $R_{expt} = 5.92\%$, $R_B = 4.08\%$, $R_M = 9.24\%$
$k_2 = (0.5, 0, 0.5)$; irrep: $\mathbf{\Gamma_7}$
$Fe1_1$: C1 = −2.08(14), C2 = 2.45(14), C3 = C4 = 0, $\delta = 0.125$, $M = (-1.47(9),0,1.73(9))\mu_B$
$Fe2_1$: C1 = 2.08(14), C2 = −2.45(14), C3 = C4 = 0, $\delta = 0.125$, $M = (1.47(9),0,-1.73(9))\mu_B$
$Ho1_1$: C1 = 3.56(17), C2 = 1.72(41), C3 = C4 = 0, $\delta = 0.22(1)$, $M = (3.52(3),0,1.70(8))\mu_B$
$Ho2_1$: C1 = −1.31(12), C2 = 0.93(21), C3 = C4 = 0, $\delta = 0.32(2)$, $M = (1.20(5),0,-0.85(9))\mu_B$

$T = 3$ K: $\chi^2 = 4.74$, $R_p = 9.40\%$, $R_{wp} = 11.2\%$, $R_{expt} = 5.13\%$, $R_B = 5.74\%$, $R_M(k_2) = 5.46\%$, $R_M(k_3) = 8.04\%$
$k_2 = (0.5, 0, 0.5)$; irrep: $\mathbf{\Gamma_7}$
$Fe1_1$: C1 = −4.55(9), C2 = 2.54(13), C3 = C4 = 0, $\delta = 0.125$, $M = (-3.20(6),0,1.51(9))\mu_B$
$Fe2_1$: C1 = 4.55(9), C2 = −2.54(13), C3 = C4 = 0, $\delta = 0.125$, $M = (3.20(6),0,-1.51(9))\mu_B$
$Ho1_1$: C1 = 3.43(21), C2 = −6.40(5), C3 = C4 = 0, $\delta = 0.131(6)$, $M = (2.85(14),0,4.95(3))\mu_B$
$Ho2_1$: C1 = 2.70(1), C2 = 4.52(11), C3 = C4 = 0, $\delta = 0.218(5)$, $M = (-3.00(1),0,4.15(2))\mu_B$
$k_3 = (0, 0, 0.5)$; irrep: $\mathbf{\Gamma_2}$ with a combination of Ψ_{21} and Ψ_{22} basic vectors

$Fe1_1$: C1 = 1.41(20), C2 = 1.41(20), C3 = C4 = 0, $\delta = 0.08(5)$, $M = (0,1.24(18),0)\mu_B$
$Fe2_1$: C1 = −1.41(20), C2 = −1.41(20), C3 = C4 = 0, $\delta = 0.09(3)$, $M = (0,-1.24(18),0)\mu_B$
$Ho1_1$: C1 = 0.97(35), C2 = −3.78(25), C3 = C4 = 0, $\delta = 0$, $M = (0,0.97(35),0)\mu_B$
$Ho2_1$: C1 = 4.69(32), C2 = 2.03(35), C3 = C4 = 0, $\delta = 0.03(1)$, $M = (0,4.62(31),0)\mu_B$

Position of magnetic ions: $Fe1_1$ (0.0317,0.75,0.2122); $Fe2_1$ (0.1889,0.25,0.0242); $Ho1_1$ (0.5869,0.75,0.9874); $Ho2_1$ (0.3570,0.75,0.8091). Magnetic phases δ are in units of 2π.

for the determined k_2 value and the *Pnma* space group, eight irreps are predicted for the 4*c* site: $\mathbf{\Gamma} = 1\mathbf{\Gamma_1} + 2\mathbf{\Gamma_2} + 2\mathbf{\Gamma_3} + 1\mathbf{\Gamma_4} + 1\mathbf{\Gamma_5} + 2\mathbf{\Gamma_6} + 2\mathbf{\Gamma_7} + 1\mathbf{\Gamma_8}$, as summarized in Table IV. Notably, within all the irreps in Table IV, all four magnetic Fe or Ho ions at the 4*c* sites are coupled by magnetic symmetries. Similarly, the values of ordered moments and magnetic phases

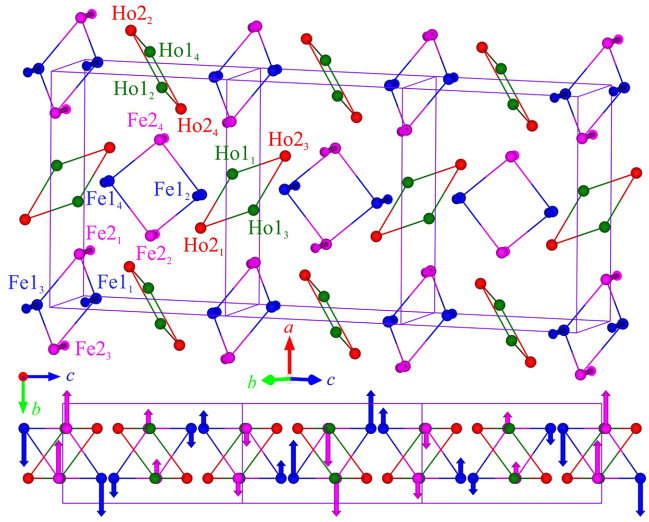

FIG. 5. Scheme of the incommensurate magnetic structure with $k_1 = (0, 0, 0.329)$ at 42 K in $BaHoFeO_4$.

of Fe1 and Fe2 ions inside the same ring are constrained to be identical, while these parameters are refined independently for Ho1 and Ho2 ions. It has been established that the magnetic structure corresponding to irrep $\mathbf{\Gamma_7}$ best and satisfactorily describes the observed magnetic contributions. Notably, the irrep observed for the k_2 magnetic phase in $BaHoFeO_4$ differs from irrep $\mathbf{\Gamma_3}$ reported by Dönni *et al.* for the magnetic phase with the same k_2 propagation vector in isostructural $BaErFeO_4$ [5]. The refined parameters of the CM magnetic phase are presented in Table III, and its details are outlined in Fig. 6. It is characterized by the ferromagnetic (FM) alignment between Fe1 or Fe2 ions inside the same rings; however, the coupling between Ho1 or Ho2 ions inside their rings is AFM. All the ordered Fe and Ho moments are located in the *ac* plane.

As shown in Fig. 6, at $T = 25$ K, Fe ions form a collinear AFM spin configuration within the Fe_4O_{18} rings. The ordered magnetic moments of the Fe ions remain consistent across different rings. The moments are lying in the *ac* plane, and they are nearly parallel to the basal oxygen plane of the $Fe2O_6$ octahedra and perpendicular to the Fe1O axial bonds of the $Fe1O_5$ square pyramids. This configuration can be attributed to the large single-ion anisotropy within the FeO pyramids and strong AFM intrachain interactions. In contrast, the Ho ions exhibit a noncollinear ordered structure within their respective rings. The magnitude of the ordered Ho moments varies between different chains depending on the phase factor. There is a large magnetic phase difference between Ho1 and Ho2 inside each ring of Ho ions (Table III). Notably, the magnetic

TABLE IV. Irreducible representations (IR) and Basis vectors (BsV) for the 4*c* sites of Fe and Ho atoms in the *Pnma* space group with the magnetic propagation $k = (0.5, 0, 0.5)$: $\mathbf{\Gamma} = 1\mathbf{\Gamma_1} + 2\mathbf{\Gamma_2} + 2\mathbf{\Gamma_3} + 1\mathbf{\Gamma_4} + 1\mathbf{\Gamma_5} + 2\mathbf{\Gamma_6} + 2\mathbf{\Gamma_7} + 1\mathbf{\Gamma_8}$. All four magnetic ions on site 4*c* are coupled by magnetic symmetry.

IR	BsV	*x,y,z*	$-x+0.5, -y, z+0.5$	$-x, y+0.5, -z$	$x+0.5, -y+0.5, -z+0.5$
$\mathbf{\Gamma_1}$	Ψ_1	Re (0 1 0)	(0 0 0)	(0 1 0)	(0 0 0)
		Im (0 0 0)	(0 1 0)	(0 0 0)	(0 1 0)
$\mathbf{\Gamma_2}$	Ψ_{21}	Re (1 0 0)	(0 0 0)	(−1 0 0)	(0 0 0)
		Im (0 0 0)	(1 0 0)	(0 0 0)	(−1 0 0)
	Ψ_{22}	Re (0 0 1)	(0 0 0)	(0 0 −1)	(0 0 0)
		Im (0 0 0)	(0 0 −1)	(0 0 0)	(0 0 1)
$\mathbf{\Gamma_3}$	Ψ_{31}	Re (1 0 0)	(0 0 0)	(1 0 0)	(0 0 0)
		Im (0 0 0)	(1 0 0)	(0 0 0)	(1 0 0)
	Ψ_{32}	Re (0 0 1)	(0 0 0)	(0 0 1)	(0 0 0)
		Im (0 0 0	(0 0 −1)	(0 0 0)	(0 0 −1)
$\mathbf{\Gamma_4}$	Ψ_4	Re (0 1 0)	(0 0 0)	(0 −1 0)	(0 0 0)
		Im (0 0 0)	(0 1 0)	(0 0 0)	(0 −1 0)
$\mathbf{\Gamma_5}$	Ψ_5	Re (0 1 0)	(0 0 0)	(0 1 0)	(0 0 0)
		Im (0 0 0)	(0 −1 0)	(0 0 0)	(0 −1 0)
$\mathbf{\Gamma_6}$	Ψ_{61}	Re (1 0 0)	(0 0 0)	(−1 0 0)	(0 0 0)
		Im (0 0 0)	(−1 0 0)	(0 0 0)	(1 0 0)
	Ψ_{62}	Re (0 0 1)	(0 0 0)	(0 0 −1)	(0 0 0)
		Im (0 0 0)	(0 0 1)	(0 0 0)	(0 0 −1)
$\mathbf{\Gamma_7}$	Ψ_{71}	Re (1 0 0)	(0 0 0)	(1 0 0)	(0 0 0)
		Im (0 0 0)	(−1 0 0)	(0 0 0)	(−1 0 0)
	Ψ_{72}	Re (0 0 1)	(0 0 0)	(0 0 1)	(0 0 0)
		Im (0 0 0)	(0 0 1)	(0 0 0)	(0 0 1)
$\mathbf{\Gamma_8}$	Ψ_8	Re (0 1 0)	(0 0 0)	(0 −1 0)	(0 0 0)
		Im (0 0 0)	(0 −1 0)	(0 0 0)	(0 1 0)

moments of Ho ions show a tendency to align parallel with their neighboring Fe spins; for example, Ho1 aligns with Fe1, and Ho2 aligns with Fe2 (Fig. 5). It suggests strong FM Ho-Fe superexchange interactions, which are facilitated by large values of the Ho-O-Fe bond angles: approximately 158° for the Ho1-Fe1 pairs and 164° for Ho2-Fe2 pairs. These observations highlight the dominant role of the 3*d*-4*f* sublattice interaction in inducing the magnetic ordering of the Ho ions.

Upon cooling to 15 K, the ordered magnetic moments of Fe ions and $Ho1_1$/$Ho1_3$ ions gradually increase, with insignificant deviations from their initial directions. In contrast, both

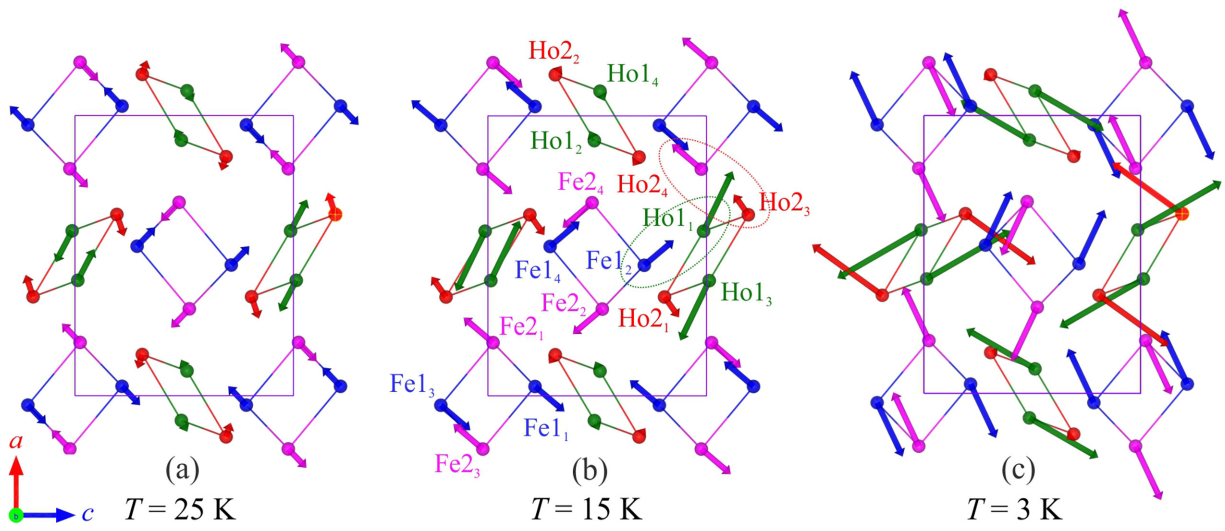

FIG. 6. Evolution of the commensurate magnetic structure with k_2 with temperature in $BaHoFeO_4$.

TABLE V. Irreducible representations for the 4*c* sites of Fe and Ho in the *Pnma* space group with the magnetic propagation $k = (0, 0, 0.5)$: $\mathbf{\Gamma} = 4\mathbf{\Gamma_1}+2\mathbf{\Gamma_2}$. All four magnetic ions on site 4*c* are coupled by magnetic symmetry.

IR	BsV		x, y, z	$-x+0.5, -y, z+0.5$	$-x, y+0.5, -z$	$x+0.5, -y+0.5, -z+0.5$
$\mathbf{\Gamma_1}$	Ψ_{11}	Re	(1 0 0)	(0 0 0)	(0 0 0)	(0 0 0)
		Im	(0 0 0)	(1 0 0)	(0 0 0)	(0 0 0)
	Ψ_{12}	Re	(0 0 1)	(0 0 0)	(0 0 0)	(0 0 0)
		Im	(0 0 0)	(0 0 −1)	(0 0 0)	(0 0 0)
	Ψ_{13}	Re	(0 0 0)	(0 0 0)	(−1 0 0)	(0 0 0)
		Im	(0 0 0)	(0 0 0)	(0 0 0)	(−1 0 0)
	Ψ_{14}	Re	(0 0 0)	(0 0 0)	(0 0 −1)	(0 0 0)
		Im	(0 0 0)	(0 0 0)	(0 0 0)	(0 0 1)
	Ψ_{15}	Re	(0 0 0)	(0 0 0)	(−1 0 0)	(0 0 0)
		Im	(0 0 0)	(0 0 0)	(0 0 0)	(1 0 0)
	Ψ_{16}	Re	(0 0 0)	(0 0 0)	(0 0 −1)	(0 0 0)
		Im	(0 0 0)	(0 0 0)	(0 0 0)	(0 0 −1)
	Ψ_{17}	Re	(1 0 0)	(0 0 0)	(0 0 0)	(0 0 0)
		Im	(0 0 0)	(−1 0 0)	(0 0 0)	(0 0 0)
	Ψ_{18}	Re	(0 0 1)	(0 0 0)	(0 0 0)	(0 0 0)
		Im	(0 0 0)	(0 0 1)	(0 0 0)	(0 0 0)
$\mathbf{\Gamma_2}$	Ψ_{21}	Re	(0 1 0)	(0 0 0)	(0 0 0)	(0 0 0)
		Im	(0 0 0)	(0 1 0)	(0 0 0)	(0 0 0)
	Ψ_{22}	Re	(0 0 0)	(0 0 0)	(0 1 0)	(0 0 0)
		Im	(0 0 0)	(0 0 0)	(0 0 0)	(0 1 0)
	Ψ_{23}	Re	(0 0 0)	(0 0 0)	(0 1 0)	(0 0 0)
		Im	(0 0 0)	(0 0 0)	(0 0 0)	(0 −1 0)
	Ψ_{24}	Re	(0 1 0)	(0 0 0)	(0 0 0)	(0 0 0)
		Im	(0 0 0)	(0 −1 0)	(0 0 0)	(0 0 0)

the magnitude and the direction of the magnetic moments for $Ho2_1$/$Ho2_3$ ions remain nearly unchanged. Notably, the magnetic moments of $Ho1_2$/$Ho1_4$ and $Ho2_2$/$Ho2_4$ ions tend to decrease slightly upon cooling, reaching a small value of approximately $0.64(13)\mu_B$ at 15 K. Additionally, the magnetic moments obtained at 15 K are $2.27(13)\mu_B$ for Fe ions, $3.91(6)\mu_B$ for $Ho1_1$ ions, and $1.47(9)\mu_B$ for $Ho2_1$ ions (Table III). These values are significantly smaller than the spin-only values of $5.9\mu_B$ for the high-spin Fe^{3+} ion and $10.6\mu_B$ for the Ho^{3+} ion. Such an observation indicates the existence of a substantial disordered component in the Fe and Ho magnetic sublattices. Furthermore, the magnetic phase difference between Ho1 and Ho2 within the same ring, i.e., $Ho1_1$ and $Ho2_1$, decreases sharply from $\Delta\delta = 1.3\pi$ at 25 K to 0.2π at 15 K, and then remains almost unchanged upon further cooling (0.18π at 3 K) (see Table III). At 3 K, a sharp increase of the ordered magnetic moments of $Ho2_1$, $Ho2_3$, $Ho1_2$, and $Ho1_4$ ions is also observed, accompanied by an abrupt change in the directions of the ordered magnetic moments of both Ho and Fe ions. This behavior highlights the enhancement of $4f$-$4f$ interactions in the compound.

Interestingly, in the NPD pattern at 3 K, in addition to the commensurate AFM phase with $k_2 = (0.5, 0, 0.5)$, extra magnetic reflections were observed at 2θ positions of 4.28°, 8.07°, and 14.74°, as denoted in Fig. 4(d). These magnetic peaks correspond to the emergence of a new commensurate AFM order with the magnetic propagation $k_3 = (0, 0, 0.5)$. Representational analysis identified two possible irreps, $\mathbf{\Gamma} = 4\mathbf{\Gamma_1}+2\mathbf{\Gamma_2}$, as summarized in Table V. The irrep $\mathbf{\Gamma_1}$ describes the magnetic spins arranged in the *ac* plane, while the $\mathbf{\Gamma_2}$ corresponds to the spins aligned along the *b* axis. Within these irreps, all four magnetic ions on site 4*c* are coupled by magnetic symmetry. Data analysis indicates that the magnetic structure with k_3 corresponds to $\mathbf{\Gamma_2}$, involving a combination of the basis vectors Ψ_{21} and Ψ_{22}, with details provided in Table III. As illustrated in Fig. 7, this magnetic structure is formed predominantly due to the ordering of Ho spins. The Ho magnetic moments are aligned along the *b* axis and modulated along the *c* axis, with the maximum values of $3.78(25)\mu_B$ for Ho1 and $4.62(31)\mu_B$ for Ho2. For the Fe magnetic sublattice, similarly to refinements of the other magnetic structures, the magnetic moments of the Fe^{3+} ions within the same Fe_4O_{18} ring were constrained to be the same; however, their magnetic phase factors were refined independently. It has been revealed that the magnetic configuration of Fe rings remains consistent with those observed for the magnetic structures associated with k_1 and k_2 (Table III). Notably, at 3 K, the values of ordered magnetic moments vary between 3.60(12) and $3.75(14)\mu_B$ for Fe1 and Fe2 ions, 4.70(15) and $6.85(27)\mu_B$ for Ho1 ions, and 0.64(29) and $6.90(23)\mu_B$ for Ho2 ions, indicating the persistence of strong magnetic disorder in the Ho sublattices.

C. Magnetic field and temperature-dependent Mössbauer spectroscopy

Furthermore, the evolution of the microscopic magnetic properties of $BaHoFeO_4$ was systematically investigated using Mössbauer spectroscopy. The room-temperature Möss-

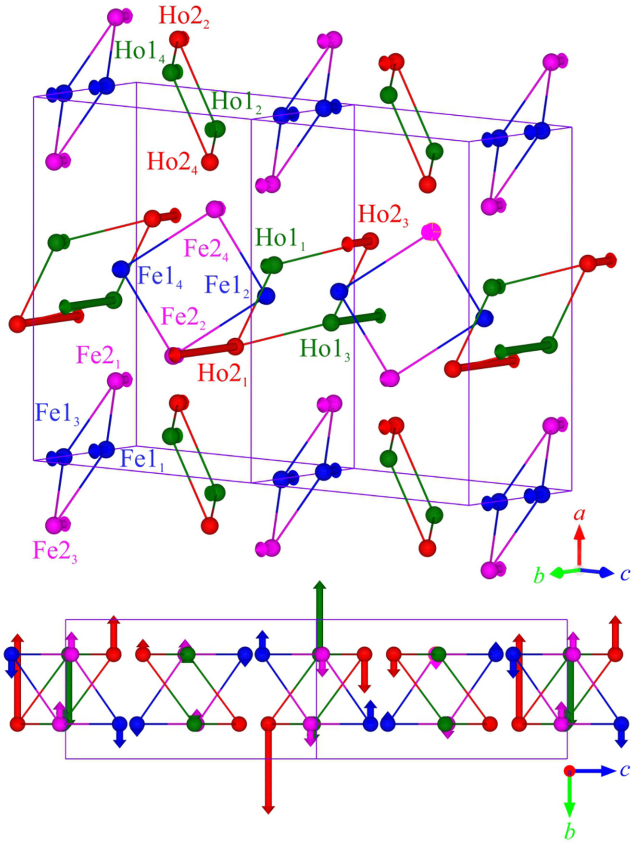

FIG. 7. Scheme of the commensurate magnetic structure with $k_3 = (0, 0, 0.5)$ at 3 K in $BaHoFeO_4$.

bauer spectrum, recorded at 4 mm/s velocity sweep, consists of two doublets, D_1 and D_2, with close isomer shifts (IS) of 0.37(1) and 0.29(1) mm/s but markedly different quadrupole splittings (QS) of 0.26 and 0.47 mm/s, respectively [Fig. 8(a) and Table VI]. These parameters are indicative of paramagnetic high-spin Fe^{3+} ions, with D_1 (higher IS) corresponding to Fe2 in the octahedra $Fe2O_6$ and D_2 attributed to Fe1 in square pyramids $Fe1O_5$. This assignment aligns with the general trend of a decrease of IS with decreasing coordination of Fe atoms in FeO_n polyhedra [7,18]. The larger QS value for the D_2 doublet indicates a higher principal component V_{zz} of the electric field gradient (EFG) at the square pyramidal $Fe1O_5$ site compared to the octahedral $Fe2O_6$ site, consistent with those reported for the $BaRFeO_4$ system [1,2,7]. To assess the sample purity, an additional room-temperature spectrum was recorded using a wider velocity sweep 12 mm/s [Fig. 8(b)]. A low-intensity sextet S_3 ($I \sim 3\%$) was detected, characterized by hyperfine parameters IS = 0.40(6) mm/s, QS = −0.04(9) mm/s, and hyperfine magnetic field at ^{57}Fe nuclei $\mu_0 H_{hf} = 49.8(6)$ T matching those reported for the orthorhombic $HoFeO_3$ [19,20], confirming the presence of this impurity as indicated by the diffraction data.

Upon cooling, below T_{N1}, the Mössbauer spectra demonstrate the emergence of magnetic sextets, signaling the onset of magnetic ordering of Fe ions (Fig. 9). At 43 K, the spectrum was modeled using a single sextet with a very broad distribution of H_{hf}, indicative of the formation of spin-density waves of the Fe magnetic moments [1,7]. Within the SDW phase, the Fe magnetic moments μ_{Fe} exhibit significant variation, causing corresponding fluctuations in H_{hf}, which can be approximated by the relation $\mu_0 H_{hf}$ (T)$\approx 11 \mu_{Fe}$ (μ_B) [1,7,21]. The H_{hf} variations dominate over the differences in hyperfine parameters between the two Fe crystallographic sites, necessitating the use of a single sextet with a wide H_{hf} distribution and an averaged IS to fit the experimental spectrum [see inset of Fig. 9(a)].

Below T_{N2}, the Mössbauer spectrum at 30 K can be decomposed into two sextets S1 [IS = 0.50(3) mm/s, QS = −0.11(3) mm/s, $\mu_0 H_{hf} = 35.1(3)$ T] and S2 [IS = 0.39(4) mm/s, QS = 0.01(6) mm/s, $\mu_0 H_{hf} = 34.0(4)$ T] with a broad hyperfine magnetic field distribution $\mu_0 \Delta H_{eff} = 3.7(2)$ T and $\mu_0 \Delta H_{eff} = 10.8(5)$ T, corresponding to the octahedral and pyramidal Fe sites, respectively [Fig. 9(b)]. The line intensity ratio in the fitted sextets is $I_{1,6} : I_{2,5} : I_{3,4} = 3 : b : 1$, with $b \approx 2$, which is typical for a homogeneously random orientation of the magnetic moments of Fe^{3+} ions in powder samples [7]. Below T_{Ho}, at 20 K, the spectral features become significantly narrower, and the magnetic sextets become well separated with relatively narrow distributions; for example, $\mu_0 \Delta H_{eff}$ is 2.4(2) T and 1.9(2) T for the octahedral S1 and pyramidal S2 sextets, respectively. At 10 and 4.2 K, the distributions become even narrower [$\mu_0 \Delta H_{eff} = 0.8(3)$ T] for both sites. The Mössbauer parameters for all selected temperatures are summarized in Table VI. The small doublet D3 is related to

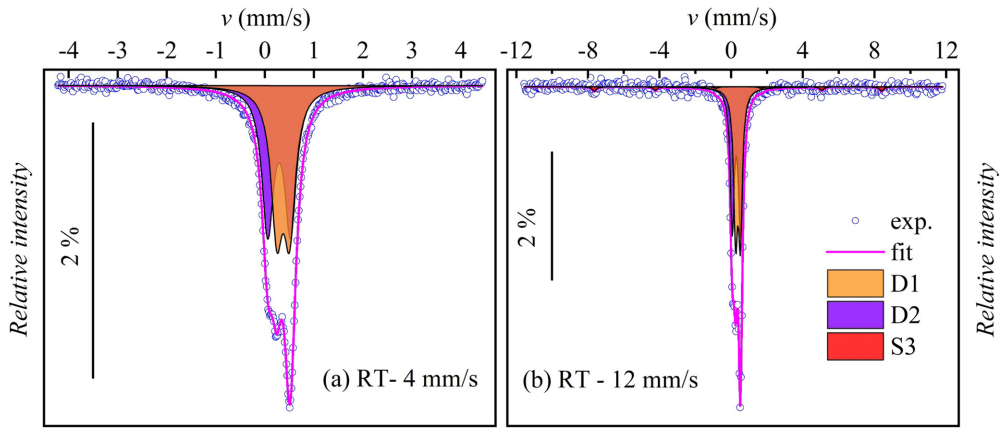

FIG. 8. Room-temperature Mössbauer spectrum of $BaHoFeO_4$ at velocity sweep of 4 mm/s (a) and 12 mm/s (b).

TABLE VI. Hyperfine parameters determined from the ^{57}Fe Mössbauer spectra of $BaHoFeO_4$. The parameter designations: H, external magnetic field; IS, isomer shift; QS, quadrupole splitting (shift); $\langle H_{\rm eff}\rangle$, mean value of effective magnetic field on ^{57}Fe nuclei $H_{\rm eff} = |\boldsymbol{H}_{\rm hf} - \boldsymbol{H}_{\rm ext}|$; I, intensity; Γ, linewidth; $\Delta H_{\rm eff}$, distribution width of effective magnetic field. Components: S1,S1a, octahedral site; S2,S2a, pyramidal site; S3, $HoFeO_3$; and D3, Al foil (0.5% Fe). Parameters marked with an asterisk (*) are fixed.

T, H	Comp.	IS (mm/s)	QS (mm/s)	$\langle H_{\rm eff}\rangle$ (T)	I (%)	b	Γ (mm/s)	$\Delta H_{\rm eff}$ (T)
300 K	D1	0.38(2)	0.27(2)		48(1)		0.26(1)	
	D2	0.28(2)	0.46(2)		49(1)		0.26(1)	
	S3	0.40(6)	−0.04(9)	49.8(6)	3(1)	2.0*	0.27*	∼0
53 K	D1	0.52(3)	0.27(4)		48(1)		0.35(2)	
	D2	0.43(3)	0.47(4)		48(1)		0.35(2)	
	S3	0.6(1)	−0.3(2)	54.1(9)	4(2)	2.0*	0.27*	∼0
43 K	S1, S2	0.44(6)	−0.10(6)	12 (6)	92(2)	2.0*	0.27*	∼12
	S3	0.51(7)	−0.17(9)	54.8(5)	3(1)	2.0*	0.27*	∼0
	D3	0.34(4)	0.39(5)		4(1)		0.27*	
30 K	S1	0.50(3)	−0.11(3)	35.1(3)	46(1)	2.06(4)	0.30*	3.7(2)
	S2	0.39(4)	0.01(6)	34.0(4)	46(1)	2.06(4)	0.30*	10.8(5)
	S3	0.46(5)	−0.25(7)	54.5(4)	4(1)	2.0*	0.27*	∼0
	D3	0.28(3)	0.39(4)		4(1)		0.27*	
20 K	S1	0.51(3)	0.05(4)	41.5(3)	46(1)	2.11(4)	0.30(1)	2.4(2)
	S2	0.41(3)	−0.19(4)	40.3(3)	46(1)	2.11(4)	0.30(1)	1.9(2)
	S3	0.45(6)	−0.20(9)	54.7(5)	4(1)	2.0*	0.27*	∼0
	D3	0.33(4)	0.30(6)		4(1)		0.27*	
10 K	S1	0.51(3)	0.02(3)	45.1(3)	46(1)	2.10(6)	0.26(1)	0.7(3)
	S2	0.43(3)	−0.15(3)	43.5(3)	46(1)	2.10(6)	0.26(1)	0.8(3)
	S3	0.54(6)	−0.31(17)	54.1(5)	4(1)	2.0*	0.27*	∼0
	D3	0.24(5)	0.54(8)		4(1)		0.27*	
4.2 K	S1	0.51(2)	0.05(3)	45.9(3)	47(1)	2.05(3)	0.26(1)	0.7(1)
	S2	0.42(2)	−0.18(3)	44.4(3)	48(1)	2.05(3)	0.26(1)	0.8(1)
	S3	0.46(5)	−0.10(7)	54.6(5)	3(1)	2.0*	0.27*	∼0
	D3	0.37(7)	0.45(9)		2(1)		0.27*	
4.2 K; 0.5 T	S1	0.51(3)	0.05(4)	45.7(3)	46(1)	1.92(6)	0.30(1)	0.9(3)
	S2	0.42(3)	−0.15(4)	44.2(3)	46(1)	1.92(6)	0.30(1)	0.9(3)
	S3	0.40(7)	−0.01(9)	53.2(5)	3(1)	2.0*	0.27*	∼0
	D3	0.43(5)	0.30(8)		4(1)		0.27*	
4.2 K; 1.0 T	S1	0.52(3)	0.07(4)	45.5(3)	46(1)	1.87(5)	0.28(1)	2.1(2)
	S2	0.41(3)	−0.16(4)	44.1(3)	46(1)	1.87(5)	0.28(1)	1.5(2)
	S3	0.42(7)	0.11(9)	55.3(5)	3(1)	2.0*	0.27*	∼0
	D3	0.38(5)	0.33(7)		4(1)		0.27*	
4.2 K; 2.0 T	S1	0.49(3)	−0.01(4)	45.9(3)	47(1)	1.77(4)	0.29(1)	3.0(3)
	S2	0.43(3)	−0.11(4)	43.5(3)	47(1)	1.77(4)	0.29(1)	2.6(2)
	S3	0.52(7)	0.26(9)	53.8(5)	3(1)	2.0*	0.27*	∼0
	D3	0.25(5)	0.53(7)		3(1)		0.27*	
4.2 K; 6.0 T	S1	0.51*	0.11(8)	45.5(6)	25(3)	1.43(6)	0.29(1)	6.2(9)
	S1a	0.51*	0.07(4)	49.4(3)	25(3)	2.7(2)	0.29(1)	2.7(4)
	S2	0.42*	−0.26(8)	44.5(7)	25(3)	1.43(6)	0.29(1)	6.5(9)
	S2a	0.42*	−0.02(4)	39.9(4)	25(3)	2.7(2)	0.29(1)	3.5(4)

iron impurity in the aluminum foil (0.5% Fe) that covers the detector.

It is worth noting that the broad spectral lines and the associated distribution of $H_{\rm hf}$ are attributed to the following two factors: First, the orientation of the hyperfine field vector is distributed relative to the local structural environment, which leads to a distribution in QS, described by $\mathrm{QS} = \frac{1}{4}eQV\mathrm{zz}(3\cos^2\theta - 1 + \eta\sin^2\theta\cos 2\phi)$, where η is the asymmetry parameter of the EFG tensor, Q is the quadrupole moment of the ^{57}Fe nuclei, and θ and ϕ are the polar and azimuthal angles of $H_{\rm hf}$ relative to the EFG tensor's principal axis system. Second, there is a distribution of $H_{\rm hf}$ caused by the anisotropy of the hyperfine interaction. Both effects naturally arise from the noncollinear arrangement of Fe magnetic moments, which is consistent with the magnetic structures derived from the neutron diffraction data. In the fitting procedure, the effects of the noncollinear magnetic structure were modeled considering the distribution of the $H_{\rm hf}$ magnitudes only, keeping the angles θ and ϕ as the nondistributed parameters.

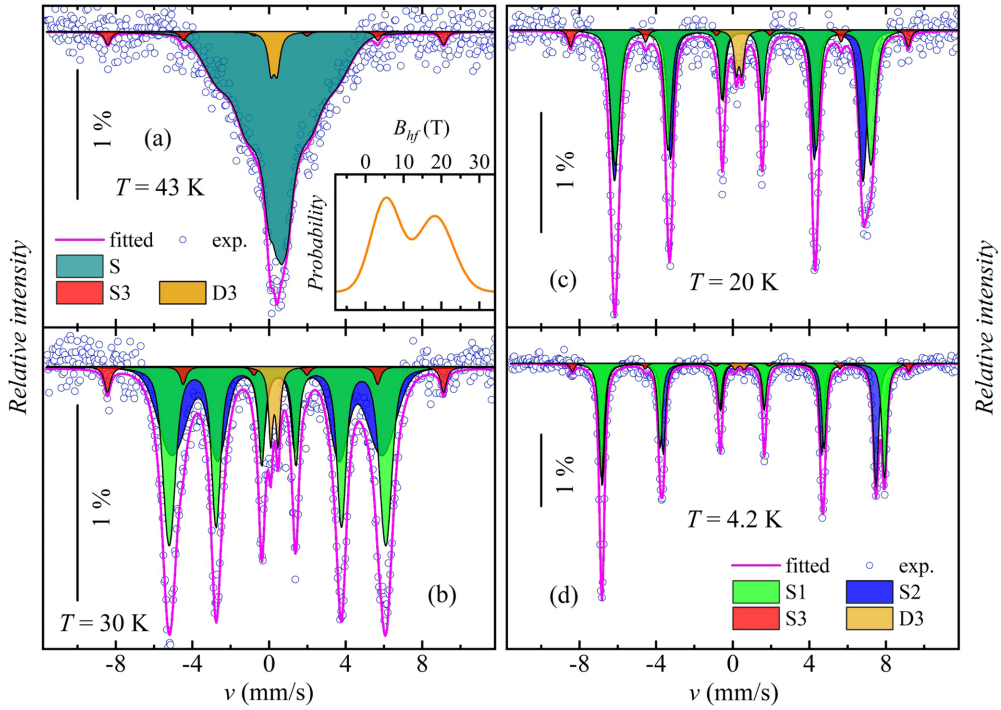

FIG. 9. Mössbauer spectrum of $BaHoFeO_4$ at selected low temperatures 43 K (a), 30 K (b), 20 K (c), and 4.2 K (d). Inset of (a): Distribution of hyperfine magnetic field at ^{57}Fe nuclei.

To gain insight into the effects of the magnetic field on the magnetic ordering of Fe spins, additional Mössbauer spectra were collected at 4.2 K under various H, as shown in Fig. 10. The in-field spectra at 0.5, 1, and 2 T retain the same features as the zero-field spectrum, but with a decrease in the relative intensities of the second and fifth lines (i.e., the parameter b). This change reflects a variation in the mean angle $\langle\theta_m\rangle$ between the direction of the γ rays and the effective magnetic field at the Fe nucleus H_{eff}, described by the relationship $b = 4\sin^2\langle\theta_m\rangle/(1+\cos^2\langle\theta_m\rangle)$ [7,22,23]. Specifically, $b = 2$ corresponds to $\langle\theta_m\rangle = 54.74°$ (randomly oriented moments in the powder sample), while $b = 0$ and $b = 4$ correspond

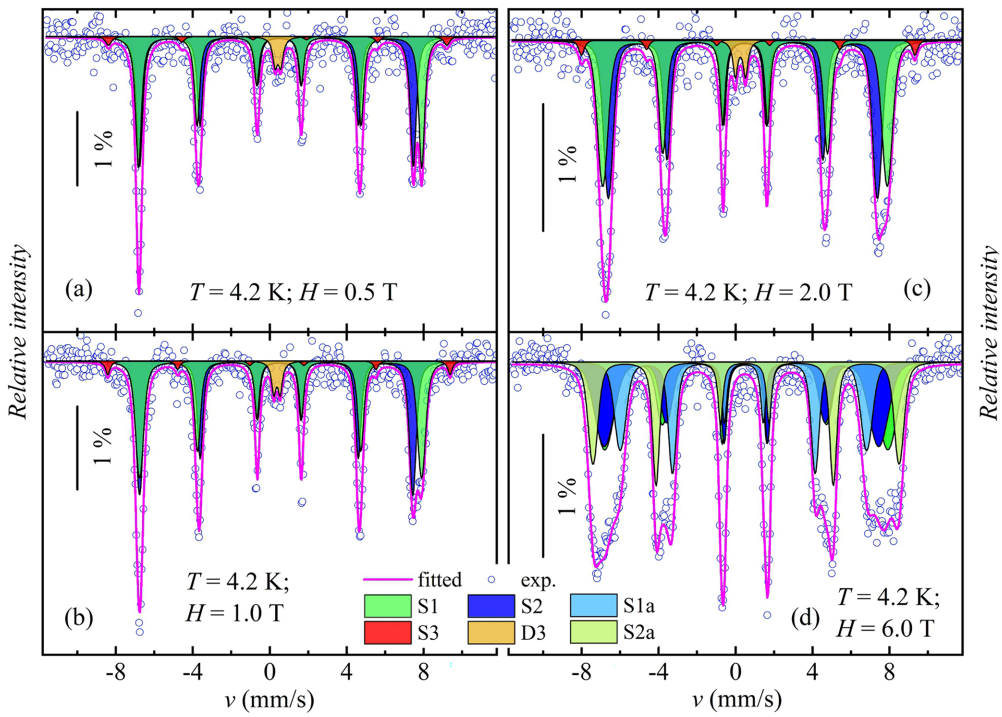

FIG. 10. Mössbauer spectrum of $BaHoFeO_4$ at 4.2 K under external magnetic field 0.5 T (a), 1 T (b), 2 T (c), and 6 T (d).

to $\langle\theta_m\rangle = 0$ and 90°, respectively, representing H_{eff} being completely parallel and perpendicular to the γ rays. As shown in Table VI, as $\mu_0 H$ increases from 0.5 to 2 T, the value of b gradually and linearly decreases from 1.92(6) to 1.77(4), corresponding to a decrease in $\langle\theta_m\rangle$ from 53.6(8)° to 52.9(6)°. This means an H-induced rotation of Fe^{3+} moments towards the direction of the γ rays, i.e., away from the external magnetic field.

However, at $\mu_0 H = 6$ T, the sextets become broader and split into two sextets for each Fe site [Fig. 10(d)]. The fitting results yielded one type of sextets (S1,S2) with $b = 1.43(6)$ and another type (S1a,S2a) with $b = 2.7(2)$ with the same relative intensity. Notably, the value of $\langle\theta_m\rangle$ of 46.5(9)°, corresponding to $b = 1.43(6)$, closely aligns with the extrapolated linear fit of the $\langle\theta_m\rangle$ values reported for S1 and S2 sextets at lower magnetic fields. Therefore, the sextets with $b < 2$ at $\mu_0 H = 6$ T are likely associated with the initial phase, whose Fe spins are rotated towards the direction of the γ rays under the application of $\mu_0 H \leqslant 2$ T. Furthermore, the latter case with $b > 2$ corresponds to $\langle\theta_m\rangle = 65.8(3)°$, meaning that the Fe^{3+} spins deviate by 24.2(3)° from the direction of the external magnetic field. Additionally, as shown in Table VI, $\mu_0 H_{eff}$ of S1a for the octahedral site increases by about 4.5 T, while $\mu_0 H_{eff}$ of S2a for the pyramidal site decreases by the same amount. Under an applied field of 6 T, the pyramidal Fe spins tend to align parallel to the direction of the external magnetic field, while the octahedral Fe spins orient antiparallel. These observations highlight the robustness of the zero-field initial spin configuration of the $[Fe_4O_{18}]$ column with AFM correlation between neighboring Fe ions in the field-induced magnetic phase, consistent with that reported for $BaYFeO_4$ [7]. Hence, the AFM $[Fe_4O_{18}]$ columns can be considered as magnetic units in the analysis of the magnetic properties of BaRFeO$_4$ systems.

D. Terahertz time-domain spectroscopy

The spin dynamics of the $BaHoFeO_4$ sample was investigated using terahertz time-domain spectroscopy, a method well suited for studying magnetically ordered crystalline compounds [24,25]. To the best of our knowledge, there are no reports on terahertz spectroscopic studies involving compounds from the BaRFeO$_4$ family yet. Therefore, we have performed such measurements on $BaHoFeO_4$, as functions of temperature and magnetic field. The first series of experiments made use of an optical cryostat without magnetic field. The resulting complex refractive index spectra $N(f)$ obtained on cooling are displayed in Fig. 11. These spectra correspond to the product of the spectra of relative permittivity and permeability, $N(f) = [\mu(f)\varepsilon(f)]^{1/2}$, and they may display resonances due to phonons, magnons, or electromagnons. The most prominent features are observed in the spectral range between 0.2 and 0.6 THz. At the lowest temperature of 10 K, the spectra exhibit three sharp resonances peaking at 0.3, 0.4, and 0.5 THz which, as we show below, correspond to magnon excitations reflecting the specific spin configuration of the material. A significant drop in the peak intensities occurs as the temperature exceeds T_{N1}, with further weakening observed upon further heating. Nevertheless, the three lines persist in the spectra up to $T = 200$ K, with their

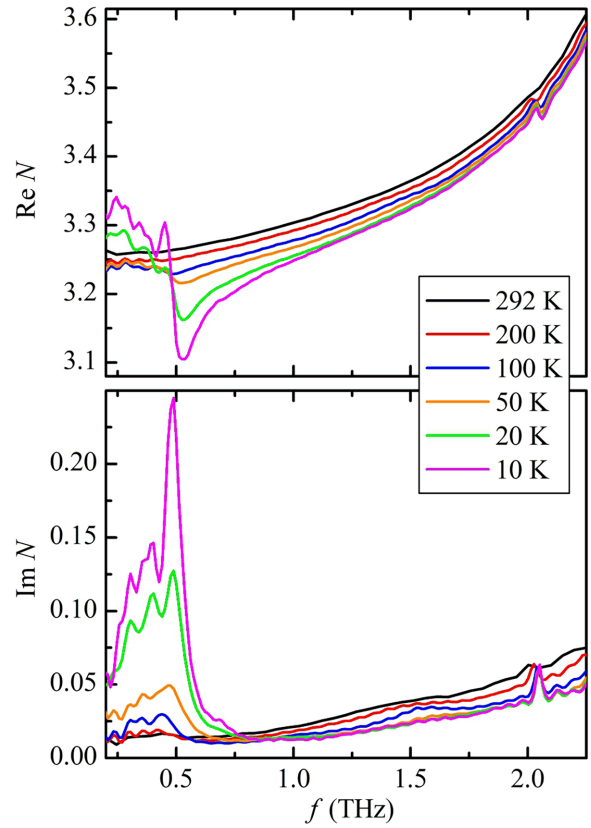

FIG. 11. Temperature dependence of the complex refractive index of $BaHoFeO_4$ measured by time-domain terahertz spectroscopy.

resonance frequencies slightly decreasing upon heating. These lines above T_{N1} are most likely attributable to paramagnons, indicating short-range magnetic ordering even in the paramagnetic phase. Due to the polycrystalline nature of the sample, no conclusions can be drawn regarding the polarization of the magnons relative to the crystal lattice. Additionally, two weaker spectral features are observed near the frequencies of 1.5 and 2 THz. Upon cooling, the intensity of the excitation at 1.5 THz slightly increases down to 100 K, becoming very weak at lower temperatures. In contrast, the excitation at 2 THz gradually strengthens with cooling, and its frequency slightly increases. However, these frequencies were not detectable in our experiments with an applied magnetic field (as discussed below), challenging current understanding. Finally, the overall increase in the refractive index towards the higher frequencies is undoubtedly due to excitations located above the upper spectral limit of our apparatus, most probably phonons.

Furthermore, the second series of experiments was focused on studying the terahertz spectra of $BaHoFeO_4$ in magnetic fields to verify whether the spectral features depend on the magnetic structure of the compound. Based on the results of magnetization measurements reported by Kumar and Sundaresan [3] showing that the *ac* susceptibility exhibits the highest frequency dependence at $T = 13$ K, this temperature value, corresponding to the CM AFM phase with the magnetic propagation vector k_2, was selected for the magnetic-field-dependent experiments. The resulting spectra of the complex

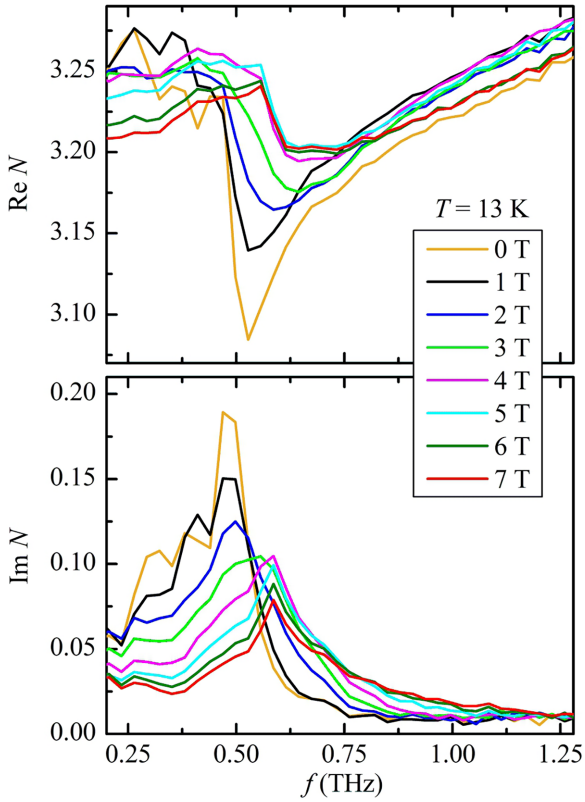

FIG. 12. Complex refractive index spectra of $BaHoFeO_4$ measured by time-domain terahertz spectroscopy at $T = 13$ K as a function of applied magnetic field.

refractive index are presented in Fig. 12. Although the frequency resolution was somewhat lower compared to that in previous measurements due to a different experimental protocol, three excitations with peak frequencies of 0.3, 0.4, and 0.5 THz are discernible in the zero-field spectra, particularly in the imaginary part. A magnetic field was applied parallel to the propagation direction of the radiation (Faraday geometry), in steps of 1 T. The aforementioned three peaks remain visible at the field value of $\mu_0 H = 1$ T, beyond which the two lower-frequency peaks gradually weaken with increasing H, and the lowest-frequency peak becomes substantially smeared at 2 T. Additionally, a new magnon peak around 0.6 THz emerges at 2 T, indicative of the onset of a new magnetic phase. With further increasing H, the field-induced mode grows at the expense of the zero-field modes, becoming the dominant feature above 4 T. The overall broadening of the spectrum at the high magnetic fields might be an indication of disorder, or of a distribution of various magnetic configurations.

IV. DISCUSSION

The observed magnetic phenomena in $BaHoFeO_4$ can be explained by the following scenario. As mentioned above, for BaRFeO$_4$ systems, the strong AFM Fe1-O-Fe2 superexchange interactions result in a collinear AFM arrangement and equivalent relative orientation of the ordered Fe moments inside each Fe chain across all magnetic structures. The diversity of magnetic states in these systems is associated with the orientation of the magnetic moments of the Fe chains with respect to each other, which is governed by the interchain magnetic interactions connecting them. The strength of the interchain magnetic interactions depends on the magnetic nature and size of the R^{3+} ions. For nonmagnetic Y^{3+}, the interchain interactions are weak super-superexchange ones mediated through Fe-O-O-Fe pathways [7,9]. The interplay of these pathways gives rise to a strong magnetic frustration, leading to the formation of complex incommensurate AFM orders in $BaYFeO_4$ [7,9,11]. Conversely, the presence of magnetic R^{3+} ions introduces new interchain superexchange Fe-O-R-O-Fe pathways, which effectively relieve magnetic frustration. In the case of $BaHoFeO_4$, strong FM Ho-O-Fe superexchange interactions, combined with strong AFM interactions between Ho spins within their rings, result in a strong AFM coupling between the chains along the a and c axes, stabilizing the commensurate AFM order with the propagation vector k_2.

Regarding the nature of the H-induced ferroelectricity in $BaHoFeO_4$, Kumar and Sundaresan observed the emergence of the H-induced ferroelectric phase above the critical magnetic field $H_1 = 1$ T, occurring strictly around T_{Ho} [3]. Furthermore, this phase develops as H increases to the critical point $H_2 = 2.3$ T and is subsequently suppressed with further increasing H, disappearing above 5 T [3]. Notably, the changes in the ferroelectric properties coincide with the critical fields associated with the spin-flop transitions in the Ho sublattice. Therefore, it provides evidence that the spin-driven ferroelectricity in $BaHoFeO_4$ is primarily related to the H-induced modifications in the Ho sublattice. This scenario is also supported by two facts. First, the collinear AFM configuration of the [Fe_4O_{18}] columns remains robust under applied magnetic fields. Second, the spin-driven ferroelectric phase in $BaYFeO_4$, which is associated with the Fe sublattice, was found to be monotonously suppressed under magnetic fields [8].

According to the spin-flop model [16,17], the Ho AFM pairs would rotate toward the direction perpendicular to the applied magnetic field when $H \leqslant H_1$, which explains the tendency of the Fe^{3+} moments to turn away from the external magnetic field, as revealed by the aforementioned Mössbauer measurements. As $H > H_1$, the initial antiparallel alignment of Ho ions within the respective ring would be perturbed, becoming canted. According to the spin-current model [26,27], this canting may break the inversion symmetry and induce electric dipoles within each Ho ring, which might be the origin of the H-induced ferroelectricity in $BaHoFeO_4$ [3]. Furthermore, the magnetization, Mössbauer, and terahertz domain spectroscopy results of this study indicate the emergence of an H-induced paraelectric phase, characterized by the FM alignment of Ho spins within their rings, as H increases to H_2. Upon further increasing H, this higher-H paraelectric magnetic phase grows at the expense of the lower-H ferroelectric magnetic phase, which may explain the observed suppression of the ferroelectricity. Further in-field neutron diffraction measurements would be useful to determine in more detail the precise spin configurations of these H-induced magnetic phases, shedding light on the discussed mechanism of the magnetoelectric coupling in the $BaHoFeO_4$ system.

V. CONCLUSIONS

In summary, the mechanisms underlying the complex magnetic phase transitions in $BaHoFeO_4$ mediated by variation of temperature and magnetic field have been systematically investigated by the combination of neutron diffraction, macroscopic magnetic measurements, Mössbauer spectroscopy, and terahertz time-domain spectroscopy. A collinear incommensurate SDW AFM order of Fe spins with the magnetic propagation vector $k_1 = (0, 0, 0.329)$ was observed below $T_{N1} \approx 50$ K. Strong intrachain superexchange interactions between Fe1 and Fe2 spins lead to a collinear AFM configuration of Fe spins within their chains, which remains robust against temperature and magnetic field changes. Below 25 K, the $3d$-$4f$ coupling transforms the SDW structure into a commensurate AFM structure with $k_2 = (0.5, 0, 0.5)$, where all Fe and Ho spins lie within the *ac* plane. This phase is characterized by essentially noncollinear magnetic order with a large magnetic phase difference between Ho1 and Ho2 spins within the same Ho chains. As temperature decreases further, the enhanced $4f$-$4f$ interactions gradually reduce the magnetic phase difference within the Ho chains and result in the emergence of a collinear commensurate AFM order with $k_3 = (0, 0, 0.5)$ at 3 K, coexisting with the k_2 phase. In this phase, the Ho and Fe magnetic moments are aligned along the *b* axis and modulated along the *c* axis. The magnetic structure within the Ho chains in the k_3 phase differs significantly from that in the k_2 phase. Under applied magnetic field, $BaHoFeO_4$ exhibits two metamagnetic phase transitions at $\mu_0 H_1 \approx 1$ T and $\mu_0 H_2 \approx 2$ T, corresponding to the starting and ending points of a spin-flop transition of the Ho magnetic sublattice. The appearance of ferroelectricity above H_1 in $BaHoFeO_4$ is proposed to be linked to the H-induced magnetic phase, characterized by a canted magnetic structure in the Ho chains. Beyond H_2, a new paraelectric magnetic phase emerges, characterized by the FM alignment of Ho spins within their rings. The suppression of ferroelectricity at higher fields can be attributed to the growth of this paraelectric phase at the expense of the low-H ferroelectric magnetic phase.

ACKNOWLEDGMENTS

The authors of the paper express their gratitude to Glazkov V. P. for helping with the neutron diffraction experiment on the DISK diffractometer of the IR-8 reactor (National Research Center "Kurchatov Institute"). This work has been funded by Vietnam National Foundation for Science and Technology Development (NAFOSTED) under Grant No. 103.02-2021.70 and the Czech Science Foundation (GAČR) under Grant No. 25-16097S. We also acknowledge the financial support by European Union and by the Czech Ministry of Education, Youth and Sports (Project TERAFIT—CZ.02.01.01/00/22_-008/0004594).

DATA AVAILABILITY

The data that support the findings of this article are not publicly available because they contain commercially sensitive information. The data are available from the authors upon reasonable request.

[1] I. S. Glazkova, A. A. Belik, A. V. Sobolev, M. N. Smirnova, N. S. Ovanesyan, and I. A. Presniakov, Modulated magnetic structures in BaRFeO$_4$(R = Y and Dy): Magnetic and ^{57}Fe Mössbauer investigations, J. Phys. Chem. C **124**, 13374 (2020).

[2] A. A. Belik, A. Dönni, M. Tanaka, I. S. Glazkova, A. V. Sobolev, and I. A. Presniakov, Different magnetic and magnetodielectric behavior of BaRFeO$_4$ ferrites with R = Ho, Er, Tm, and Yb, J. Alloys Compd. **922**, 166297 (2022).

[3] R. Kumar and A. Sundaresan, Unveiling a hidden multiferroic state under magnetic fields in $BaHoFeO_4$, Phys. Rev. B **107**, 184420 (2023).

[4] A. Dönni, V. Y. Pomjakushin, K. Yamaura, and A. A. Belik, Cycloidal spiral magnetic structures in the spin-chain compounds BaRFeO$_4$(R = Yb and Tm): Ordered Yb versus partly ordered Tm, Phys. Rev. B **107**, 134412 (2023).

[5] A. Dönni, V. Y. Pomjakushin, and A. A. Belik, Er-driven incommensurate to commensurate magnetic phase transition of Fe in the spin-chain compound $BaErFeO_4$, Phys. Rev. B **109**, 064403 (2024).

[6] C. H. Prashanth *et al.*, Interplay of magnetic and electric coupling across the spin density wave to conical magnetic ordering in a $BaHoFeO_4$ spin-cluster chain compound, J. Alloys Compd. **942**, 169017 (2023).

[7] D. P. Kozlenko *et al.*, Competing magnetic states in multiferroic $BaYFeO_4$: A high magnetic field study, Phys. Rev. Mater. **5**, 044407 (2021).

[8] J. Z. Cong, S. P. Shen, Y. S. Chai, L. Q. Yan, D. S. Shang, S. G. Wang, and Y. Sun, Spin-driven multiferroics in $BaYFeO_4$, J. Appl. Phys. **117**, 174102 (2015).

[9] E. E. Gordon, S. Derakhshan, C. M. Thompson, and M. H. Whangbo, Spin-density wave as a superposition of two magnetic states of opposite chirality and its implications, Inorg. Chem. **57**, 9782 (2018).

[10] S. Ghara and A. Sundaresan, Coexistence of long-range cycloidal order and spin-cluster glass state in the multiferroic $BaYFeO_4$, J. Phys.: Condens. Matter **30**, 245802 (2018).

[11] C. M. Thompson, J. E. Greedan, V. O. Garlea, R. Flacau, M. Tan, P. T. Nguyen, F. Wrobel, and S. Derakhshan, Partial spin ordering and complex magnetic structure in $BaYFeO_4$: A neutron diffraction and high temperature susceptibility study, Inorg. Chem. **53**, 1122 (2014).

[12] J. Rodríguez-Carvajal, Recent advances in magnetic structure determination by neutron powder diffraction, Phys. B **192**, 55 (1993).

[13] T. Žák and Y. Jirásková, CONFIT: Mössbauer spectra fitting program, Surf. Interface Anal. **38**, 710 (2006).

[14] Z. Klencsár, E. Kuzmann, and A. Vértes, User-friendly software for Mössbauer spectrum analysis, J. Radioanal. Nucl. Chem. **210**, 105 (1996).

[15] F. Wrobel, M. C. Kemei, and S. Derakhshan, Antiferromagnetic spin correlations between corner-shared $[FeO_5]^{7-}$ and $[FeO_6]^{9-}$ units, in the novel iron-based compound: $BaYFeO_4$, Inorg. Chem. **52**, 2671 (2013).

[16] A. N. Bogdanov, A. V. Zhuravlev, and U. K. Rößler, Spin-flop transition in uniaxial antiferromagnets: Magnetic phases, reorientation effects, and multidomain states, Phys. Rev. B **75**, 094425 (2007).

[17] H.-F. Li, Possible ground states and parallel magnetic-field-driven phase transitions of collinear antiferromagnets, npj Comput. Mater. **2**, 16032 (2016).

[18] F. Menil, Systematic trends of the ^{57}Fe Mössbauer isomer shifts in (FeO_n) and (FeF_n) polyhedra. Evidence of a new correlation between the isomer shift and the inductive effect of the competing bond *T*-*X* (→ Fe) (Where X is O or F and T any element with a formal posit, J. Phys. Chem. Solids **46**, 763 (1985).

[19] V. J. Angadi, K. Manjunatha, S. P. Kubrin, A. T. Kozakov, A. G. Kochur, A. V. Nikolskii, I. D. Petrov, S. I. Shevtsova, and N. H. Ayachit, Crystal structure, valence state of ions and magnetic properties of $HoFeO_3$ and $HoFe_{0.8}Sc_{0.2}O_3$ nanoparticles from x-ray diffraction, x-ray photoelectron, and Mössbauer spectroscopy data, J. Alloys Compd. **842**, 155805 (2020).

[20] J. M. D. Coey, G. A. Sawatzky, and A. H. Morrish, Magnetization and temperature dependence of the Mössbauer spectrum shift for an insulator, Phys. Rev. **184**, 334 (1969).

[21] D. Colson, A. Forget, and P. Bonville, The Modulated Antiferromagnetic structures in multiferroic $FeVO_4$: A ^{57}Fe Mössbauer spectroscopy investigation, J. Magn. Magn. Mater. **378**, 529 (2015).

[22] B. W. Dale, *Mössbauer Spectroscopy* (Springer, Berlin, Heidelberg, 1975), Vol. 5.

[23] D. Peddis, M. V. Mansilla, S. Mørup, C. Cannas, A. Musinu, G. Piccaluga, F. D'Orazio, F. Lucari, and D. Fiorani, Spin-canting and magnetic anisotropy in ultrasmall $CoFe_2O_4$ nanoparticles, J. Phys. Chem. B **112**, 8507 (2008).

[24] C. Kadlec, V. Goian, K. Z. Rushchanskii, P. Kužel, M. Lžaić, K. Kohn, R. V. Pisarev, and S. Kamba, Terahertz and infrared spectroscopic evidence of phonon-paramagnon coupling in hexagonal piezomagnetic $YMnO_3$, Phys. Rev. B **84**, 174120 (2011).

[25] F. Kadlec *et al.*, Electromagnon in the *Z*-type hexaferrite $(Ba_xSr_{1-x})_3Co_2Fe_{24}O_{41}$, Phys. Rev. B **94**, 024419 (2016).

[26] H. Katsura, N. Nagaosa, and A. V. Balatsky, Spin current and magnetoelectric effect in noncollinear magnets, Phys. Rev. Lett. **95**, 057205 (2005).

[27] Y. Tokura, S. Seki, and N. Nagaosa, Multiferroics of spin origin, Rep. Prog. Phys. **77**, 076501 (2014).